



# A node-splitting lattice spring model coupled with a $J$ -integral formulation as a fracture criterion

Bo Ye · Espen Jettestuen ·  
Anders Malthe-Sørenssen

Received: 8 March 2023 / Accepted: 9 October 2023  
© The Author(s) 2023

**Abstract** A global energy minimization criterion based on Griffith's theory is introduced for the node-splitting lattice spring model. The fracture criterion is computed by both direct numerical simulations of energy release rate  $G$  and through a  $J$ -integral formulation for comparison and validation. For mode I fractures, the standard implementation of  $J$ -integral formulation yields very good estimations of the energy release rate, but for mixed mode fracture the estimations deviates from the direct calculated energy release rate. The reasons for this discrepancy are elucidated and an approach to best approximate the  $J$  value is given. This method is compared with the more standard maximum tip stress threshold crack criterion, and shows a much better prediction of the energy release rate and is more robust under grid refinement.

**Keywords** Node-splitting · Lattice spring model · Sub-critical fracture growth · Global energy criterion · Local stress criterion · Energy release rate ·  $J$ -integral ·  $J_2$  path dependency

---

E. Jettestuen  
NORCE-Research, Nygårdsgaten 112, 5008 Bergen,  
Norway  
e-mail: esje@norceresearch.no

B. Ye (✉) · A. Malthe-Sørenssen  
Department of Physics, University of Oslo, P.O. Box 1048,  
Blindern, 0316 Oslo, Norway  
e-mail: boy@student.matnat.uio.no

A. Malthe-Sørenssen  
e-mail: anders.malthe-sorensen@fys.uio.no

## 1 Introduction

Lattice spring model (LSM) is a type of discrete element model widely used in fracture mechanics (Hafver et al 2014; Flekkøy et al 2002; Malthe-Sørenssen et al 1998; Meakin 1987; Martins et al 2018), fluid structure interaction (Buxton et al 2005; Wu and Qi 2017) and computer graphics (Selle et al 2008; Norton et al 1991) due to its efficiency in coupling continuum media to fracture networks and fluid processes. The model is made up of nodes joint by one dimensional elastic elements like Hookean springs or beams. Despite its simple structure, the modeling approach has been used to simulate complex systems like fractures in thin films (Meakin 1987), fractures of extensional clay (Malthe-Sørenssen et al 1998), rock weathering (Røyne et al 2008), hydro-fracture (Hafver et al 2014; Flekkøy et al 2002) and bending cracks in the African elephant skin (Martins et al 2018). The fracture criteria in these models are usually discrete variations of the maximum tangential stress (MTS) condition, e. g., if a spring is extended further than a predefined critical threshold. This type of fracture criterion has shown to give convincing results for crack pattern generations. The dynamics evolution of cracks predicted by LSM has also worked well when the time scale of a system is not given by the spring block model *per se* but by a secondary process like diffusion or drying. However, when we want to study a process like sub-critical crack growth (Swanson 1984; Freiman 1984; Atkinson 1984; Røyne et al 2011), where the kinetics of the system is

given by the elastic state, rigorous and accurate fracture criteria based on Griffith's energy minimization (Griffith 1921) are still absent for LSM. Although, cohesive approach of bond-breaking model are recently proposed (Zhang et al 2015; Kostaski et al 2012). But the energy release rate is implicit. The standard MTS criterion is sensitive to the grid resolution, where it scales in a power law with mesh density. They are not directly linked to the reaction rate theory that couples the fracture criteria of energy release rate to the speed of fracture propagation in sub-critical crack growth (Wan et al 1990).

Here we will derive and study the fracture criteria based on the linear elastic fracture mechanics (LEFM) for LSM, specifically the node-splitting model (Hafver et al 2014). Our goal is to base the fracture criteria in lattice spring model on the energy release rate, to show the role of mechanical work in the calculation of the effective energy release rate and demonstrate how this couple to rate determining processes. The calculation of energy release rate using the node-splitting fracture model is based on the virtual crack propagation techniques seen in other numerical methods (Hellen 1975).  $J$ -integral is an alternative equivalent method to calculate energy release rate (Rice 1968; Rice and Budiansky 1973). The unique properties of node-splitting lattice spring model provide a simple and flexible method for  $J$ -integral calculation. The  $J$ -integration path can be constructed directly on the lattice structure by connecting the existing nodes and bonds. The elastic field values such as stress tensor, displacement gradient and strain energy density for  $J$ -integration is derived solely by using the lattice node equilibrium location with simple algorithms. We will show how to include surface traction forces using Newton–Raphson methods by a quasi-static coupling to fluid pressure as an example, and show how the additional mechanical work done by the traction forces influence the  $J$ -integral implementation of the fracture criteria. We noted that this coupling scheme is simple to extend and not limited to static pressures.

We will apply this model to sub-critical crack growth, which refers to the slow growing and time dependent opening of fractures below a material's critical fracture stress (Wan et al 1990; Røyne et al 2011). The crack velocity has been shown to depend on the residue energy release rate  $\Delta G = G_e - \gamma_s$ , where  $G_e$  is the effective energy release rate and  $\gamma_s$  is the energy needed to generate new fracture surface. The evalua-

tion of energy release rate is essential to the propagation velocity profile of sub-critical cracks, and will be affected by the traction forces caused by, for instance, the presence of fluids.

In Sect. 2, we will review the node-splitting fracture model of LSM, introduce an iterative Newton–Raphson solver for equilibrium and show the numerical methods of the building blocks of fracture criteria such as stress, strain tensor. Then, we will detail the implementation of energy release rate and  $J$ -integral for LSM, beginning with traction free fracture surface in Sect. 3. To account for the external process, in Sects. 4 and 5, we will couple a static pressure as surface traction on to the fracture surface of LSM and update the fracture criteria. Finally, we will present the numerical results of the fracture criteria and its application to sub-critical fracture from Sects. 6 to 8.

## 2 Basics of node-splitting LSM

The LSMs are often used to model elastic media and consist of nodes interconnected by bonds. They can either be unstructured (Bolander Jr and Saito 1998; Ostoja-Starzewski 2002) or structured (Meakin 1987; Malthe-Sørensen et al 1998; Hafver et al 2014) and the neighbor interaction are usually modeled by linear Hookean springs. However, in some situations, beam or other elements (Schlangen and Garboczi 1996) are used to enable modeling a wider range of mechanical properties.

In this study, we will use a standard uniform triangular grid for the node structure as shown in Fig. 1. The bonds connecting nodes are linear Hookean springs with equilibrium length  $l$  and the basic building block of such a network is commonly a triangular cell. Although, a square cell can also be used as a basic block (Ostoja-Starzewski 2002). Each spring in the cell has a spring constant of  $k/2$ . An internal bond consists of edges from two neighboring cells so that the effective spring constant is  $k$ , while a boundary bond has a spring constant of  $k/2$ .

It can be shown that the continuum limit of this model represents an isotropic homogeneous elastic media with a Young's modulus  $E$  of  $2k/\sqrt{3}$  and a Poisson's ratio of  $1/3$  (Flekkøy et al 2002). We note that the Young's modulus can be adjusted by varying the spring constant, but the Poisson's ratio is fixed. If a different Poisson's ratio is required, bonds can be replaced by

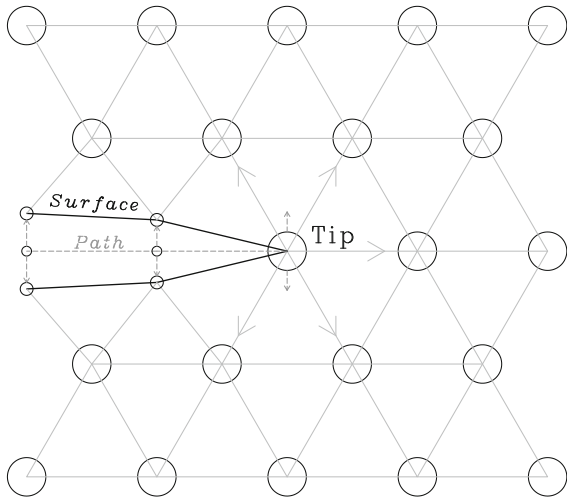


**Fig. 1** Node-splitting LSM. The label Tip refers to fracture tip, Surface means fracture surface and Path is the crack path. The grey arrows show the possible future fracture directions

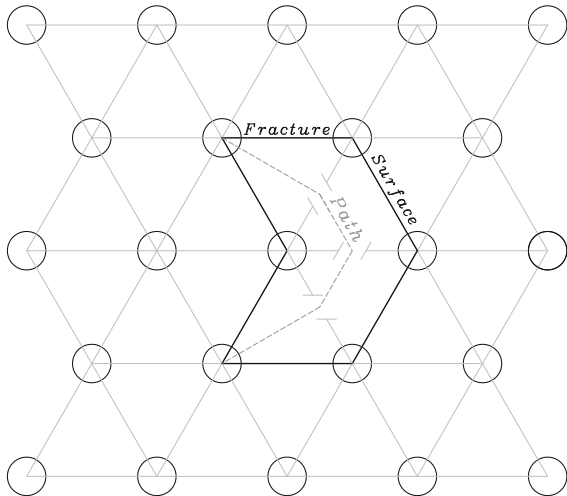


**Fig. 2** Bond-breaking LSM

a beam as previously mentioned (Schlangen and Garboczi 1996).

Bond-breaking, schematically shown in Fig. 2, is the standard method to model brittle fractures in LSM (Flekkøy et al 2002; Malthe-Sørensen et al 1998; Meakin 1987; Røyne et al 2008). In this type of model, a fracture propagates by removing bond that exceeds a predefined stress threshold. An alternative to bond-breaking is a node-splitting model (Hafver et al 2014) shown in Fig. 1. When a fracture grows, in the node-splitting model, the node at the fracture tip splits into two new nodes as indicated by the two small and oppo-

site arrows. The new fracture direction could, in principle, be in any of the five directions marked by arrows. Once the fracture direction is determined by a fracture criterion, the bond in this direction also splits and the newly split bond changes from an internal one to become a part of the fracture surface. Meanwhile, the spring constant of the two new bonds at the fracture surface is updated to  $k/2$ . The node-splitting mechanism ensures a well defined fracture volume and conservation of elastic energy unlike bond-breaking, where the potential energy of a bond is lost, when it is removed, in addition to suffer an abrupt change in fracture volume.

As previously stated, we assume that the interaction between neighboring nodes is modeled by linear elastic spring. The force on a central node, labeled as  $b$  in Fig. 3, from the spring in lattice direction  $\alpha$  is, in this case, given by

$$f_{\alpha,i} = k_{\alpha}(|\mathbf{r}_b - \mathbf{r}_{\alpha}| - l)c_{\alpha,i}. \tag{1}$$

where  $f_{\alpha,i}$  is the  $i$ 'th component of the spring force and  $i$  is Cartesian component,  $k_{\alpha}$  is the spring constant of a bond in direction  $\alpha$ ,  $\mathbf{r}_b$  and  $\mathbf{r}_{\alpha}$  are the positions of node  $b$  and its neighbor in the  $\alpha$ -direction,  $c_{\alpha,i}$  is the  $i$ 'th component of the unit vector pointing from node  $b$  to its  $\alpha$  direction neighbor node, and  $(|\mathbf{r}_b - \mathbf{r}_{\alpha}| - l)$  is the bond elongation. The accumulated spring force,  $F_{b,i}$ , on node  $b$  from its neighbors is

$$F_{b,i}(\mathbf{r}_b, \mathbf{r}_{\alpha=1}, \dots, \mathbf{r}_{\alpha=6}) = \sum_{\alpha=1}^6 f_{\alpha,i}. \tag{2}$$

For all nodes in a LSM network, to establish the equilibrium state, the sum of forces on each node must be zero, that is,  $F_{b,i} = 0$  for all nodes. Since only the equilibrium state is of interest in this study, a standard iterative Newton–Raphson method is used to solve the non-linear system. The node positions at iteration  $n + 1$  is given by  $r_i^{(n+1)} = r_i^{(n)} + \delta r_i$ , where the  $\delta r_i$  is found by solving the linear system of equations given by

$$F_{b,i}^{(n)} + \delta r_{b,j} \frac{\partial F_{b,i}}{\partial r_{b,j}} + \sum_{\alpha} \delta r_{\alpha,j} \frac{\partial F_{b,i}}{\partial r_{\alpha,j}} \Big|_{\mathbf{r}^{(n)}} = 0. \tag{3}$$

where  $F_{b,i}^{(n)}$  is the value of the sum of forces at iteration  $n$  and we have used Einstein summation convention for repeated indexes  $i$  and  $j$ .  $b$  is the label of a central node shown in Fig. 3 and  $\alpha$  indicates a neighbor. Once the equilibrium position of the nodes,  $\mathbf{r}^{eq}$ , is found, we can compute the strain,  $\varepsilon_{ij}$ , stress,  $\sigma_{ij}$ , tensor and strain energy density,  $w$ , at each node. These quanti-

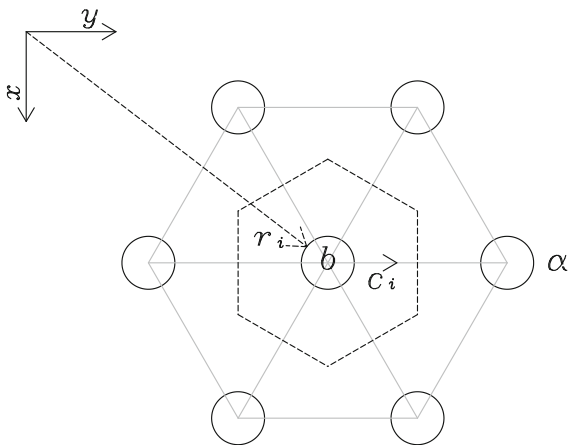


**Fig. 3** Definition of reference frame and notations of an intact internal hexagon lattice cell

ties are essential for the development of fracture criteria (Knowles and Sternberg 1972; Rice and Budiansky 1973; Bolander Jr and Saito 1998).

To illustrate how to implement the numerical scheme, we include a step by step description below. The algorithm consists of four parts. First part is simulation parameters input such as mesh resolution, spring properties, bond length. Second, a series of neighbor lists of nodes are formed such as node id, spring constant, node location. Third part is node list local modification due to fracture. Last part is the Newton–Raphson iterative solver where a linear system of equations are formed and solved by iterative method.

1. Input simulation parameters

- (a) Spring properties: stiffness  $k$ , bond length  $l$
- (b) Mesh resolution  $N$
- (c) Loading statement: strain  $\epsilon$ /stress  $\sigma$

2. Form neighbor list based on the hexagon lattice for computing neighboring spring forces

- (a) Assign a unique ID to each node and collect the node id of hexagon neighbor to a list(nid-list)
- (b) Collect stiffness of the neighboring bonds and form the corresponding list as the ID list above(k-list)
- (c) Collect the locations of neighboring nodes and form the same list(r-list)

3. Local modification of neighbor list due to node-splitting fracture

- (a) Modify nid-list,k-list and r-list according to the length of pre-existing fracture
4. Determine linear system  $J\delta r = F$  size and convert node id to linear system index for assemble
- (a) For example, node id  $n$  is converted to index as  $2n - 1$  and  $2n$  for the location of  $x$  and  $y$  components of  $\delta r$  and  $F$  in  $J$  matrix
5. Newton–Raphson solver loop
- (a) Compute gradient  $\frac{\partial F_{b,i}}{\partial r_{b,j}}$  and force  $F_{b,i}^{(n)}$  terms for each node
  - (b) Assemble force and gradient terms in to the linear system  $J\delta r = F$  according to the index
  - (c) Solve the linear system using an iterative solver
  - (d) Update the location of node toward equilibrium  $r_i^{(n+1)} = r_i^{(n)} + \delta r_i$
  - (e) Break loop when the threshold of L2 norm of error is reached
6. Post processing: e.g. Energy release rate,  $J$ -integral

For a 2d grid where the third dimension is implicit, the stress tensor  $\sigma_{ij}$  at internal node  $b$  is approximated based on the forces from the neighboring bonds in the following manner (Flekkøy et al 2002; Hafver et al 2014; Landau and Lifshitz 1986)

$$\sigma_{ij} \approx \frac{1}{2\sqrt{3}l} \sum_{\alpha=1}^6 (c_{\alpha,i} f_{\alpha,j} + c_{\alpha,j} f_{\alpha,i}). \tag{4}$$

The stress at nodes on the fracture surface, as shown in Fig. 4, follows the same formula except that the prefactor becomes  $\frac{1}{\sqrt{3}l}$  due to the reduced number of neighbors.

The displacement gradient  $u_{i,j} = \frac{\partial u_i}{\partial x_j}$  is computed from the Taylor expansion of the displacement vectors  $u_i = r_i^{eq} - r_i^0$

$$\Delta r_{\alpha,j} \frac{\partial u_i}{\partial x_j} \approx u_{\alpha,i} - u_{b,i}. \tag{5}$$

where  $u_{b,i}$  and  $u_{\alpha,i}$  are the displacement vectors of node  $b$  and its  $\alpha$  neighbor and  $\Delta r_{\alpha,j} = r_{\alpha,i}^{eq} - r_{b,i}^{eq}$ . The displacement gradient is calculated by solving the over-determined system of linear equation using the least-squares approximation. The strain tensor  $\epsilon_{ij}$  is computed based on the displacement gradient  $u_{i,j}$  (Landau and Lifshitz 1986; Sadd 2009)

$$\epsilon_{ij} = \frac{1}{2}(u_{i,j} + u_{j,i}). \tag{6}$$

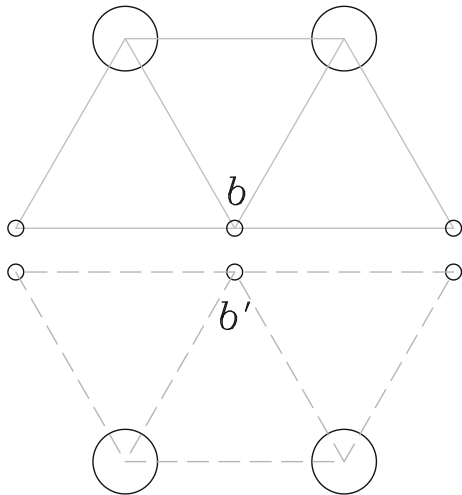


**Fig. 4** A schematic of half hexagon lattice on a fracture surface

For the stress and strain tensor, the discrepancy between the numerical definitions here and theoretical values scales linearly with strain loading.

The elastic energy density  $\omega$  is computed in two ways. In the first method, we use the standard formula for the potential energy stored in a spring, and then relate half of the energy of the spring to each of the nodes connected to it. The energy density of a node  $b$  is then given by

$$\omega = \frac{1}{2A} \sum_{\alpha=1}^6 \frac{k_{\alpha}}{2} (\Delta l_{\alpha})^2. \quad (7)$$

where  $A$  is the area of the Voronoi cell, illustrated in Fig. 3 by a gray dashed line. This definition is similar to the stress equation in Eq. 4 by using the information of neighboring nodes. The energy density can also be calculated from strain and stress tensor (Landau and Lifshitz 1986; Sadd 2009) of the continuum theory as

$$\omega = \frac{1}{2} \varepsilon_{ij} \sigma_{ij}. \quad (8)$$

### 3 Introducing energy based fracture criteria to node-splitting LSM based on LEFM

LSM has been used extensively to study fractures in various settings (Meakin 1987; Malthé-Sørensen et al 1998; Røyne et al 2008; Flekkøy et al 2002; Hafver et al 2014; Martins et al 2018), where the fracture criteria are usually a variate of the maximum tangential

stress (MTS) condition. Normally, the fracture criterion is given by a predefined critical stress  $\sigma_c$  (Flekkøy et al 2002) or a critical strain  $\epsilon_c$  (Martins et al 2018), when this is exceeded, the spring breaks and is subsequently removed from the simulation. The MTS criterion has shown convincing results for pattern generations and dynamic evaluation. However, when we want to study a process such as sub-critical fracture, the kinetics depends on the energy release rate of the spring system (Wan et al 1990). MTS as a fracture criterion is no longer a valid option as it shows strong dependence on the mesh density of the spring network. As a result, it is difficult to evaluate the energy release rate from the stress intensity factor. Here, we introduce a direct calculation technique of energy release rate based on virtual crack extension to the node-splitting LSM starting with a traction free fracture surface. Meanwhile, we also show a  $J$  integral implementation as a valid alternative for comparison and validation to the direct energy release rate calculation.

#### 3.1 Implementation detail of a direct calculation of energy release rate in LSM network

Base on the virtual crack extension method, the overall energy release rate is the change of potential energy  $\Pi$  over generating a finite fresh fracture surface and is given as  $-\delta\Pi/\delta L$  (Lifeng and Korsunsky 2005), where  $\delta L$  is the length of fresh crack in 2d. Potential energy is the combination of strain energy  $E$  due to deformation and work potential  $W$  by traction forces

$$\Pi = E - W. \quad (9)$$

For simplicity, we start without any traction force such as fluid pressure on the fracture surface, the work potential vanishes and the energy release rate is purely elastic. Later, we will show a coupling scheme where the static pressure is applied on the fracture surface and its corresponding fracture criteria in Sects. 4 and 5. The potential energy is reduced to the strain energy  $E$  of the body and is shown as

$$\Pi = E = \sum w(r_{b,i})A(r_{b,i}). \quad (10)$$

where  $w$  is the elastic energy density seen in Eq. 7 and  $A$  is the area of a single Voronoi cell. The summation is over the whole body.

Considering a solid body at equilibrium with an existing fracture of length  $L$ , the strain energy is  $E_I(L)$ .



Then, the fracture virtually extends a length of  $\delta L$  which is the bond length  $l$  for LSM. The post strain energy of the body due to extension is  $E_{II}(L + \delta L)$ . Thus, the change of potential energy is

$$-\delta\Pi = -\delta E = E_I(L) - E_{II}(L + \delta L). \tag{11}$$

However, due to the discrete nature of LSM, the fracture can extend in five possible directions as indicated by the arrows in Fig. 1. These directions are refereed as  $\alpha$  previously. In  $\alpha$  direction, the solid body has a strain energy of  $E_{II}^\alpha(L + \delta L)$ . As a result, the elastic energy release rate is

$$G^\alpha(L) = (E_I(L) - E_{II}^\alpha(L + \delta L))/\delta L. \tag{12}$$

where  $G^\alpha(L)$  is the energy release rate in direction  $\alpha$ . In this model, Griffith’s fracture criterion is given by

$$G_{max} > 2\gamma_s. \tag{13}$$

where  $\gamma_s$  is the surface energy of the material and  $G_{max}$  is the maximum value among  $G^\alpha$  and the fracture direction is in  $\alpha$  direction where the maximum  $G$  occurs.

Although the direct calculation of elastic energy release rate for LSM is straight forward, it can be computationally expensive. It is because, to determine where and when a fracture propagates, we must repeatedly solve the LSM system for five times in search of the maximum  $G$ . We need an alternative method that is just as accurate but computationally efficient to determine the energy release rate.  $J$  integral is such a valid technique which we will introduce its implementation for LSM starting with traction free surface and later including external process in the following sections.

### 3.2 Implementation detail of $\mathbf{J}$ integral in LSM network

The  $J$ -integral was initially developed as a scalar quantity (Rice 1968) used in the study of mode I fracture. Later, it was generalized into a vector form by Knowles and Sternberg (1972)

$$J_i = \lim_{R \rightarrow 0} \int_{\Gamma} \left( \omega n_i - n_j \sigma_{jk} \frac{\partial u_k}{\partial x_i} \right) d\Gamma. \tag{14}$$

where  $\Gamma$  is the integration path surrounding the fracture,  $n_i$  is the outward unit vector of  $\Gamma$  and  $R$  defines the distance between the fracture tip and the location where  $\Gamma$  intersects fracture surface as depicted in Fig. 5.

A local coordinate system is schematically defined in Figs. 6 and 7 for the calculation of  $\mathbf{J}$ -integral, where  $x$  axis aligns with the fracture axial direction and the origin is placed at the fracture tip. The  $x$ -component of  $\mathbf{J}$  is equivalent to Rice (1968)’s scalar version of the  $J$ -integral. In Sect. 2, we showed how to approximate displacement gradient  $u_{i,j}$ , stress tensor  $\sigma_{ij}$ , and strain energy density  $w$  by solely using the equilibrium locations of nodes. All that is left to do is to specify a  $J$ -integration path.

Since LSM is a node-bond based model, it is natural to define  $\mathbf{J}$  integration path by a series of nodes joined by bonds as shown in Fig. 5 labeled by hexagon and elongated hexagon path. We call this type of path as on-node. Although, the implementation of a domain integral is also possible by considering the triangle cell as the integration element. Once again, the elastic field quantities such as stress, energy density and displacement gradient are known at each node. The outward normal vector  $n_i$  is calculated based on the geometry of bonds. The  $\mathbf{J}$  path integration is simply a summation process along the on-node hexagon path. In addition to the on-node integration path, off-node path with an arbitrary shape can also be constructed in LSM. As an example, see Fig. 5, where we show a circle path with the fracture tip as center. The off-node circle path is discretized as a series of straight line segments. The elastic field values are interpolated by the surrounding nodal values of LSM through radial basis function approximation. The outward unit vector is calculated based on the geometry in the same way as in on-node path. Similar to the on-node path, the off-node  $\mathbf{J}$  integration is also a summation process of the discrete segments. The distance of fracture tip and the intersection location between  $\mathbf{J}$  path and fracture surfaces is measured by  $R$  as shown in Fig. 5. In case of on-node path, due to the discrete nature of LSM, we have chosen nodes on the fracture surface as the intersection points between integration path and fracture surface.

We recognize  $n_j \sigma_{jk}$  as the surface traction,  $T_k$ , for the integration path  $\Gamma$ . The integral expression for  $J_i$  is rewritten as

$$J_i = \int_{\Gamma} \left( \omega n_i - T_k \frac{\partial u_k}{\partial x_i} \right) d\Gamma. \tag{15}$$

The surface traction can be directly calculated in LSM provided that the integration path is of on-node type. The notation follows the hexagon lattice shown in Fig. 8, where it is divided in to two parts by the integration path. For this particular setup, the traction is the

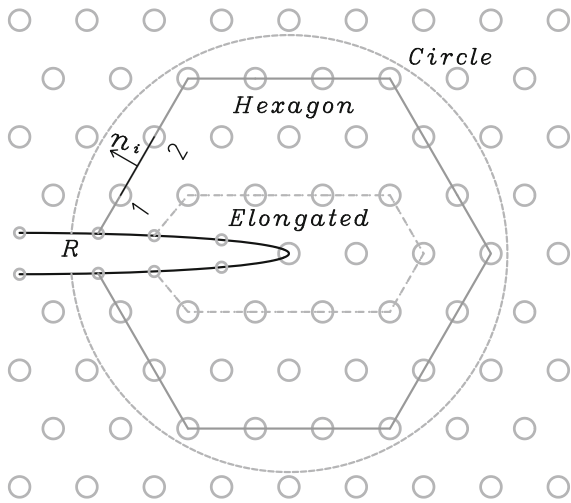


**Fig. 5** Definition of  $J$ -integration paths on a LSM grid. The hexagon and elongated hexagon path are defined by joining LSM nodes along bonds and they are called on-node type, while the circle path is one example of the off-node arbitrary path

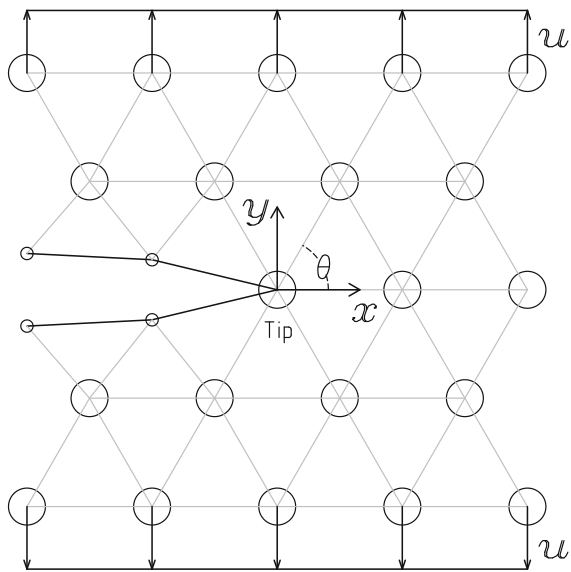


**Fig. 6** Schematics of numerical simulation setup of node-splitting LSM with a mode I fracture

summation of forces from bonds on the outward side of the integration path

$$T_i = \left( f_{3,i} + f_{4,i} + \frac{f_{2,i}}{2} + \frac{f_{5,i}}{2} \right) / l_s. \quad (16)$$

where  $l_s$  is the specific length on which traction force applies.

Lifeng and Korsunsky (2005) showed the relationship between  $\mathbf{J}$  and elastic energy release rate  $G(\theta)$

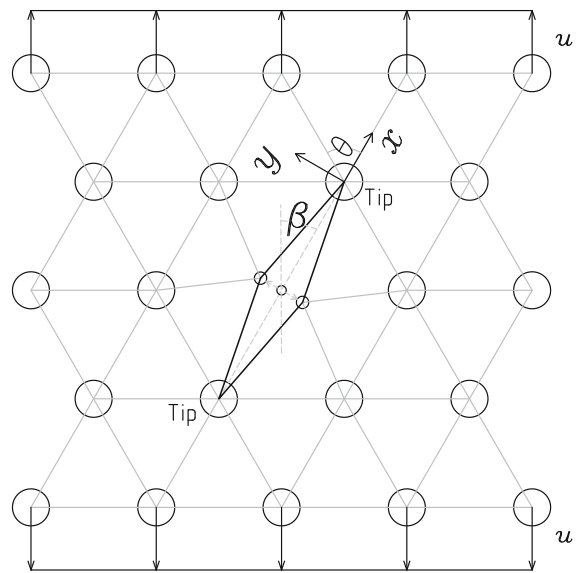


**Fig. 7** Schematics of numerical simulation setup of node-splitting LSM with a mixed mode fracture

in an arbitrary fracture direction at the fracture front given by the vector product between the unit vector  $(\cos(\theta), \sin(\theta))$  and  $\mathbf{J}$

$$G(\theta) = J_1 \cos(\theta) + J_2 \sin(\theta). \quad (17)$$

where  $\theta$  is the angle between the direction where  $G$  is measured and the  $x$ -axis of the local coordinate system as shown in Figs. 6 and 7. A positive  $\theta$  means that it is measured counter-clockwise from  $x$  axis. Given this relation, we note that the maximum value of  $G$  is found in the direction given by  $\mathbf{J}$ . Hence, it suggests that  $\mathbf{J}$  gives the fracture propagation direction with maximum energy release rate. We define  $\phi$  as the angle of  $\mathbf{J}$  vector with  $x$ -axis and it is the inverse tangent of  $J_2$  over  $J_1$ .

$$\phi = \tan^{-1} \left( \frac{J_2}{J_1} \right). \quad (18)$$

Thus, we have the maximum energy release rate as  $G_{max}(\theta = \phi) = |\mathbf{J}|$ .

#### 4 Quasi-static coupling of the LSM model to external process

To study the influence of fluid pressure on the fracture stability, we treat it as traction force and apply it as a boundary condition to LSM on the fracture surface. Here, we introduce a quasi-static coupling scheme based on the Newton–Raphson solver. For simplicity,

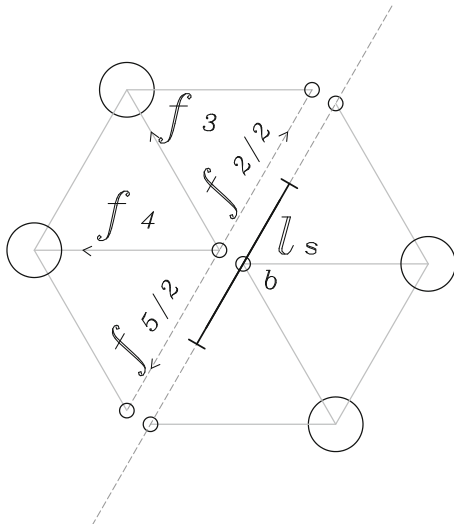


**Fig. 8** Notation for direct traction calculation on a LSM hexagon cell

we demonstrate how to couple a static uniform pressure to the node-splitting model. However, it should be noted that the scheme is generic and can be applied with a more realistic model such as a full fluid transport process.

The implementation of surface traction as a boundary condition in LSM is straight forward. Considering a surface bond with one end connected to node  $b$  and the other end connected with its neighbor node  $\alpha$  as illustrated in Fig. 3, the length of it is calculated using the node’s location

$$l' = |r_{b,i} - r_{\alpha,i}|. \tag{19}$$

The pressure force on the bond is calculated by pressure  $P$  multiplies the bond length in 2D with  $n_{\alpha,i}$  the surface norm

$$F_{\alpha,i}^f = -Pl'n_{\alpha,i}. \tag{20}$$

We distribute the pressure force on the bond equally to its associated nodes. For node  $b$ , the accumulated pressure force is

$$F_{b,i}^f = \frac{\sum F_{\alpha,i}^f}{2}. \tag{21}$$

where the summation is over the surface bonds connected to node  $b$ . The overall torque of the distributed forces at the center of the bond is zero, which is equivalent to the torque from the pressure force applied on the bond. The Newton–Raphson method seen in Eq. 3

is augmented with the variation of the pressure forces, as follow

$$F_{b,i}^{(n)} + \delta r_{b,j} \frac{\partial F_{b,i}}{\partial r_{b,j}} + \sum_{\alpha} \delta r_{\alpha,j} \frac{\partial F_{b,i}}{\partial r_{\alpha,j}} + F_{b,i}^{f(n)} + \delta r_{b,j} \frac{\partial F_{b,i}^f}{\partial r_{b,j}} + \sum_{\alpha} \delta r_{\alpha,j} \frac{\partial F_{b,i}^f}{\partial r_{\alpha,j}} \Big|_{r^{(n)}} = 0.$$

### 5 Include mechanical work to the energy release rate

To accurately account for the influence of fluids on the stability of cracks, we must include the accompanied mechanical work with the fracture growth criteria and update the  $J$  calculation with traction on the free surface. Here, we consider a mode I crack placed horizontally in the geometrical center of a solid body similar to those in Figs. 6 and 7. The equilibrium location of the node on the fracture surface prior the propagation is  $r_{b,i}^0$ . After the propagation, the equilibrium location of the same fracture surface node is  $r_{b,i}^{eq}$ . Thus, the displacement of the node is  $u_{b,i} = r_{b,i}^{eq} - r_{b,i}^0$ . The mechanical work  $W_b$  on a single node is measured by the fluid force  $F_{b,i}^f$  along the displacement  $u_{b,i}$ . The overall mechanical work  $W$  is the summation of work on all fracture surface nodes which are in contact with fluid

$$W = \sum F_{b,i}^f u_{b,i}. \tag{22}$$

Alternatively for uniform pressure, the mechanical work can be simplified further as it is proportional to the volume change of the fracture cavity due to fracture growth

$$W = P\delta_A. \tag{23}$$

where  $\delta_A$  is the fracture cavity area enlargement in 2d and  $P$  is the applied pressure. Prior to the fracture propagation, the overall cavity area is  $S_I$ . After the fracture propagation, the expanded cavity area is  $S_{II}$ .  $\delta_A$  is equal to  $S_{II} - S_I$ . We apply the general potential energy form seen in Eq. 9 to include work potential and define an effective energy release rate  $G_e$  to account for various physical processes and it is calculated as

$$G_e = (E_I - E_{II} + W)/2l. \tag{24}$$

where we previously defined the elastic energy release rate  $G = (E_I - E_{II})/2l$ . Similarly, we define mechanical energy release rate as  $G_w = W/2l$ . Thus, the effective energy release rate is the combination of elastic



energy release rate and mechanical energy release rate as  $G_e = G + G_w$ .

The fluid pressure acts as a traction  $T_i$  at the fluid solid interface. The strength of it is  $P$  for a static pressure and its direction  $n_i$  is perpendicular to the bond

$$T_i = -Pn_i. \tag{25}$$

To include the effect of traction on the fracture surface in  $J$ -integral calculation, we follow Karlsson and Bäcklund (1978)'s approach of indirectly estimating a near fracture tip  $J$  value. First, the  $J$  path is redefined by adding fracture surface segments to a  $J$  path without surface traction. The conventional traction free  $J$  path usually intersects with the fracture surface away from the fracture tip to avoid the singularity at the fracture tip. The surface segments start at the intersection location of the conventional  $J$  path and end as close to the fracture tip as possible, but not including it. Then, the  $J_i^T$  value, where the super script  $T$  implies a  $J$  calculation with traction on the fracture surface, is the addition of the combined  $J$  values on the newly defined paths

$$J_i^T(R) = J_i(R) + J_i^{ups}(R) + J_i^{lws}(R). \tag{26}$$

where  $J^s$  value of the fracture upper and lower surface segments are calculated using the traction form shown in Eq. 15 and denoted respectively by the superscripts  $ups$  and  $lws$ . In principle, the effective energy release rate  $G_e$  is also the projection of the  $J_i^T$  with traction included as shown in Eq. 17.

For uniform pressure, the  $J$  value on the fracture surface is approximately proportional (Karlsson and Bäcklund 1978) to the aperture  $\delta_c$  of the crack at the intersection location of the conventional  $J$  path with the fracture surface.

$$J^s(R) = P\delta_c. \tag{27}$$

We denote the overall  $J$  using  $J^A$  with the superscript  $A$  for approximation.

$$J^A(R) = J_i(R) + J^s(R). \tag{28}$$

## 6 Fracture growth simulations

We first show the numerical results of elastic energy release rate and the corresponding  $J$  calculation of traction free fracture surface with two cases. They are a mode I fracture and a mix mode fracture illustrated in Figs. 6 and 7, respectively. See Sect. 3 for their implementations. In both cases, we use a two dimensional

rectangular domain of size  $N_x \times N_y$  with  $N_i$  the nodal number.

The LSM system is simulated at various grid resolutions to show its convergence behavior. The horizontal and vertical nodal number are chosen to be the same with  $N \in [21, 41, 81, 161, 321, 641, 1281, 5121]$ . To simulate the same domain, the nodal number is doubled and bond length is halved from a previous grid configuration.

The system is loaded by displacing the top and bottom set of nodes in the vertical direction. The boundary nodes are free to move horizontally.

For mode I, the fracture plane is in the horizontal direction while, for the mix mode setup, it is inclined with  $\beta = 30^\circ$  from the loading direction. The crack is initiated as a split node in the middle of the sample and the physical fracture length is set to be twice the initial bond length  $l_0$ , that is  $2l_0$ . The initial configuration is with  $N = 21$ .

### 6.1 Elastic energy release rate

For mode I crack, the fracture direction is in the fracture plane. We use the notation  $G_{\theta=0^\circ}$  to denote the energy release rate in this direction defined by  $\theta = 0^\circ$  as the angular deviation from the local x-axis as shown in Fig. 6. From here on, we omit  $\theta$  for convenience.

At a fixed strain loading, the numerical results of  $G_{0^\circ}$  show three features in relation with mesh density  $N$  as seen in Fig. 9. First, it converges with the increment of mesh density, which is a property we desire. Second, the relative error defined as  $(G[i + 1] - G[i])/G[i]$  decreases proportionally with  $1/N$  i.e. error halves when resolution doubles. Third, the overall error between the  $G$  values of the lowest and the highest mesh density is within 2%, which indicates that even with a low mesh resolution, the energy release rate of Mode I fracture can be accurately calculated with LSM.

In addition, numerical  $G_{0^\circ}(\epsilon)$  agrees well with theory (Anderson 2017) as shown in Fig. 10. The linear analysis is accurate for LSM. The relative error of theoretical and numerical values are approximately the same for all strain loading. It has a quadratic growth rate with the applied strain loading  $\epsilon$  as  $G_{0^\circ} \propto \epsilon^2$  which is also shown by theory (Anderson 2017). The relationship can be seen from the log-log scale plot, where  $\log(G)$  and  $\log(\epsilon)$  has a linear relationship indicating a second order power law. The Griffith's fracture crite-

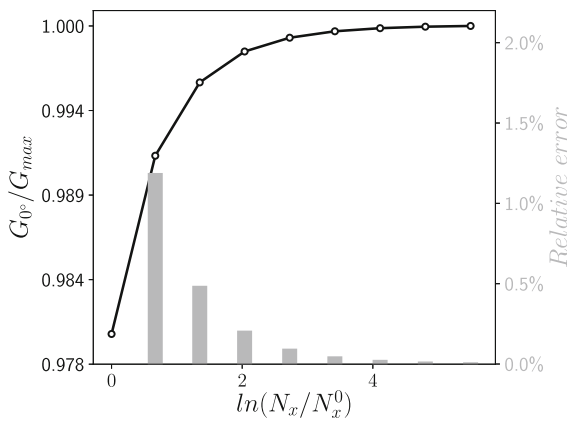


**Fig. 9** Mode I energy release rate response at various resolutions is shown on the left axis, where  $G$  is normalized to the maximum value  $G_{max}$ . On the right axis, the relative error is calculated as  $(G[i + 1] - G[i])/G[i]$  with  $i$  being a specific resolution

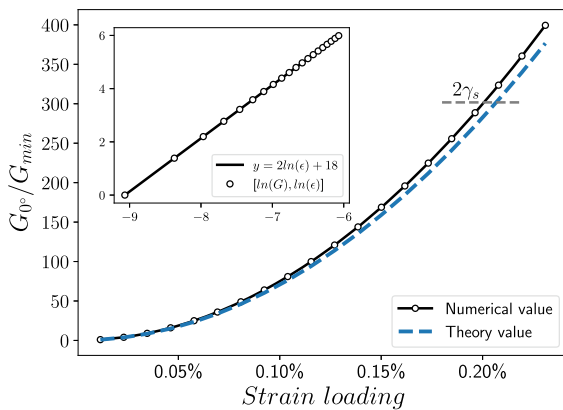


**Fig. 10** Numerical mode I energy release rate response is shown at various strain loadings, where the resolution is defined at  $\ln(N_x/N_0) = -4.15$  and  $G$  is normalized to the minimum value  $G_{min}$  at the lowest strain loading. The theoretical value of  $G_{0^\circ}$  (Anderson 2017) is shown together here

rion shown in Eq. 13 is applied when  $G_{0^\circ}(\epsilon)$  exceeds the surface energy  $2\gamma_s$ .

For a mix mode fracture, we do not usually know beforehand in which direction the maximum energy release rate is. Thus, it is necessary to search through all possible discrete directions at the fracture front marked by array in Fig. 1 to determine the direction of maximum energy release rate. However, for the setup of an inclined fracture in Fig. 7, theoretical and experimental work (Erdogan and Sih 1963) suggests that the potential fracture direction is in the direction with  $\theta = -60^\circ$ , when the inclination is at  $\beta = 30^\circ$ . We use negative sign to represent  $\theta$  below the local x-axis. As a result,

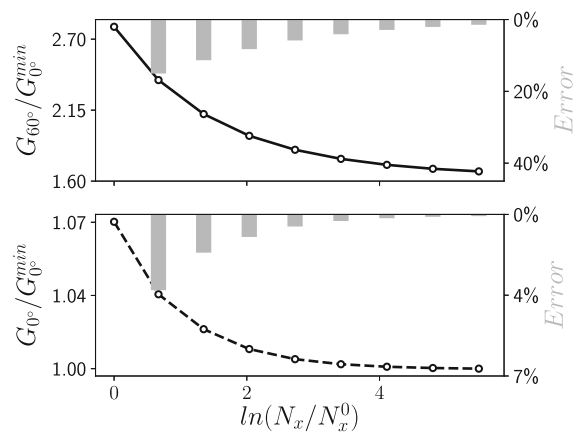


**Fig. 11** Mix mode energy release rate response at various resolutions, where  $G_{0^\circ}$  and  $G_{60^\circ}$  are normalized to  $G_{0^\circ}^{min}$ . The normalization to  $G_{0^\circ}^{min}$  compares the magnitude difference of  $G_{0^\circ}$  and  $G_{60^\circ}$  as shown by theory (Anderson 2017)

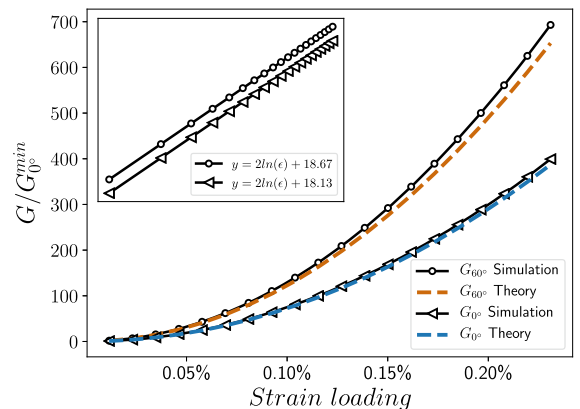


**Fig. 12** Mix mode energy release rate response at various strain loadings, where the resolution is defined at  $\ln(N_x/N_0) = -4.15$  and  $G$  is normalized to  $G_{0^\circ}^{min}$

in the simulations, we will only generate and compare results from  $\theta = -60^\circ$  and  $\theta = 0^\circ$ . From here on, we drop the negative sign to refer to the same angles.

Similar to  $G_{0^\circ}$  of the mode I fracture,  $G_{60^\circ}$  and  $G_{0^\circ}$  of mix mode show convergence over grid resolution as seen in Fig. 11. However, the error of  $G_{60^\circ}$  only decreases proportionally with  $N^{-0.6}$ . A smaller exponent indicates a slower convergence rate compared to  $G_{0^\circ}$  of both mode I and mix mode fractures who have an exponent of  $-1$ . Moreover, the error of  $G_{60^\circ}$  at low grid resolution is significant so that a high grid resolution is required to give accurate result.

The simulation values with mesh resolution  $N = 1281$  show good agreement with theoretical values as

shown in Fig. 12. The discrepancy is within a few percent and the relative error of theoretical and numerical values are approximately the same for all strain loading. Due to the faster error reduction rate, the error of  $G_{0^\circ}$  is smaller than the one of  $G_{60^\circ}$  with the same mesh resolution. The error can be further reduced with higher resolution.

With  $G_{60^\circ}(\epsilon)$  consistently a bigger value than  $G_{0^\circ}(\epsilon)$  at any  $\epsilon$ , the numerical result seen in Fig. 12 agrees with the theoretically predicted fracture direction of maximum energy release rate. Besides,  $G_{0^\circ}(\epsilon)$  and  $G_{60^\circ}(\epsilon)$  scale with the strain loading  $\epsilon$  quadratically the same way as  $G_{0^\circ}(\epsilon)$  of mode I. However,  $G_{60^\circ}(\epsilon)$  has a higher growth rate compared to  $G_{0^\circ}(\epsilon)$  as suggested by the log-log plot in Fig. 12. The higher growth rate is also the indicator that the direction with  $\theta = 60^\circ$  is the fracture direction with maximum energy release rate. The Griffith's fracture criterion in Eq. 13 is applied once  $G_{60^\circ}(\epsilon_c)$  exceeds the surface energy  $2\gamma_s$  of the material at the critical strain loading  $\epsilon_c$ .

### 6.2 Traction free $\mathbf{J}$ integral

In this section, we show the numerical results related to two properties of  $\mathbf{J}$ -integral i.e. its equivalence to the energy release rate and path independence.  $\mathbf{J}$ -integral has been considered equivalent to the energy release rate with  $G(\theta) = m_i J_i$  and  $m_i = (\cos(\theta), \sin(\theta))$  (Lifeng and Korsunsky 2005). The maximum energy release rate is in the direction of  $\mathbf{J}$  as seen in Eq. 18. Path independence is another property of  $J$ -integral (Rice 1968). To validate the path independence with LSM, we design path variations with different geometrical shapes and path intersection locations with fracture surfaces. The simulation domains and strain loading are kept the same as those in Sect. 6.1 to stay comparative.

For mode I fracture, numerical values of  $\mathbf{J}$ -integral is path independent regardless of integration path variations. In Fig. 13, two sets of  $J_1$  values are given where the path  $\Gamma$  is defined using two types of geometries with one being hexagon of equal edges and the other elongated. An illustration of the paths can be found in Fig. 5. These two value sets are identical, indicating that  $\mathbf{J}$ -integral is independent of path geometries. In addition, numerical values of  $J_1$  stay a constant in general despite of the intersection location of  $\Gamma$  with fracture surface. We can conclude that  $\mathbf{J}$ -integral is also

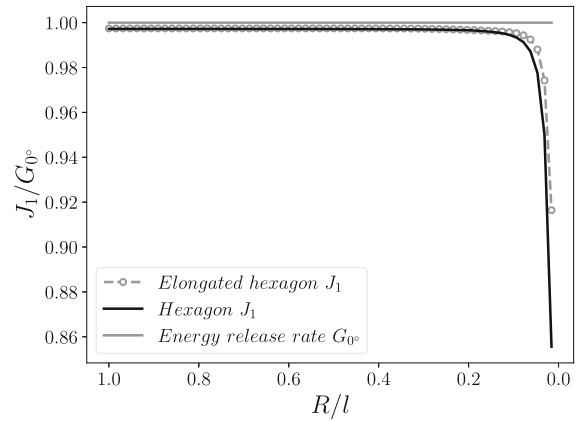


**Fig. 13** The numerical values of  $J_1(R)$  with hexagon, and elongated hexagon integration paths are shown in reference with the energy release rate of mode I fracture  $G_{0^\circ}$

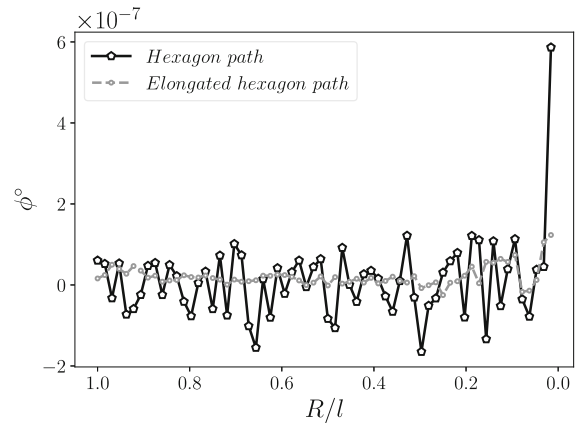


**Fig. 14** The numerical values of the directional angles as the prediction of fracture direction are shown

path independent wherever  $\Gamma$  is placed on the fracture surface. Although, we notice that  $J_1$  deviates from its constant value with  $R/l \lesssim 5\%$ , where  $R$  measures the distance between intersection location and fracture tip.

Such deviation suggests LEFM does not apply around fracture tip for LSM. One plausible explanation is that the small displacement assumption is broken as large deformation often occurs around the fracture tip. To support this assumption, as an evidence, the elastic energy density on an integration path with  $R/l \lesssim 5\%$ , seen from the lower part of Fig. 15, show discrepancy between two methods, where method II (Eq. 8) is based on small deformation while method I (Eq. 7) accounts for the energy in a deformed spring with no assumption. This discrepancy says that the continuum limit of

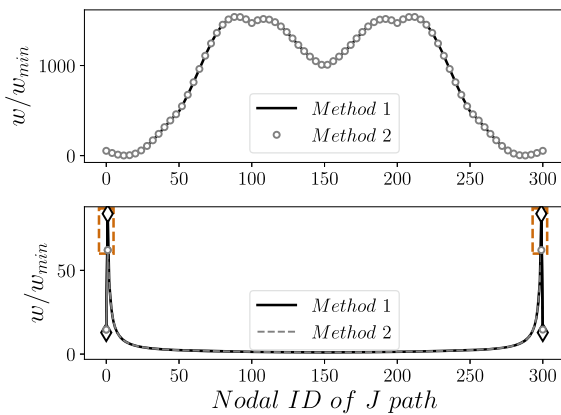


**Fig. 15** Energy density on two integration paths are given using method 1 (Eq. 7) and method 2 (Eq. 8). Path one in the upper figure intersect fracture surface away from tip, while path two in the lower figure intersect closely

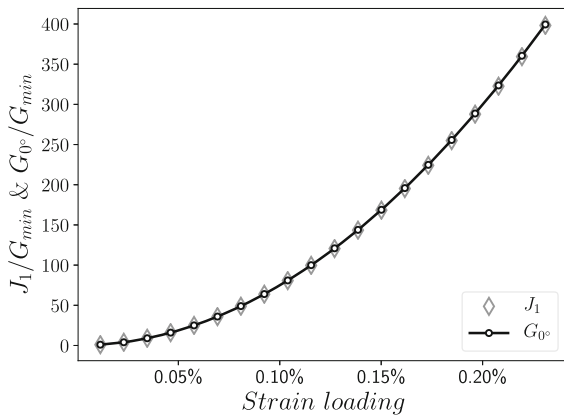


**Fig. 16**  $J_1(\epsilon)$  and  $G_{0^\circ}(\epsilon)$  of mode I are present together, where the resolution is defined at  $\ln(N_x/N_0) = -4.15$  and data is normalized to the minimum value  $G_{min}$  at the lowest strain loading

LSM as an elastic media based on small deformation no longer holds. Further more, energy densities show good match as seen from the upper part of Fig. 15 with  $R/l \gtrsim 5\%$ , where the small deformation assumption is expected to be valid and the two methods are equivalent. The two numerical methods show no superiority of accuracy over one and another. However, method I given in Eq. 7 is simpler to implement numerically.

$\mathbf{J}$  points to the right fracture direction and can be converted to the correct maximum energy release rate. The directional angle of  $\mathbf{J}$  by applying Eq. 18 is at  $\phi \approx 0$  as shown in Fig. 14, which gives the fracture direction with  $\theta = 0$ . In addition, by following Eq. 17,  $\mathbf{J}$  is converted to  $G_{0^\circ}$  as  $J_1 \cos(0^\circ) + J_2 \sin(0^\circ)$  and  $J_1$  should

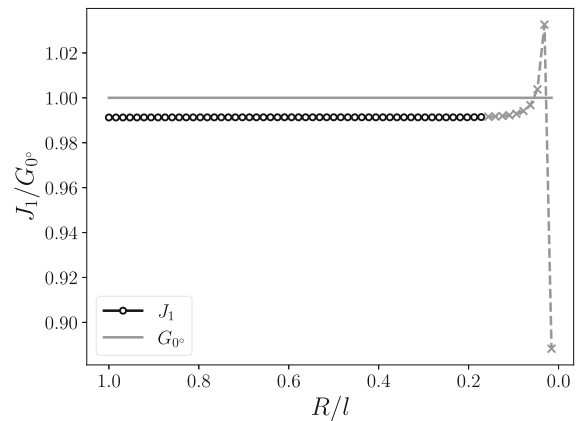


**Fig. 17** The numerical values of  $J_1(R)$  are shown in reference with  $G_{0^\circ}$  of mix mode fracture

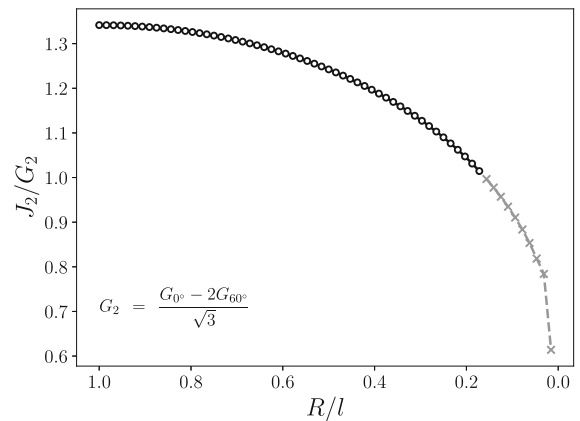


**Fig. 18**  $J_2(R)$  is shown and normalized to  $G_2 = (G_{0^\circ} - 2G_{60^\circ})/\sqrt{3}$ .  $G_2$  is the expected value of  $J_2$  given the relationship of energy release rate and  $\mathbf{J}$ -integral

be equal to  $G_{0^\circ}$ . The numerical values of  $J_1$  and  $G_{0^\circ}$  seen in Fig. 13 are similar and have less than 1% difference.

$J_1(\epsilon)$  is equivalent to the directly calculated  $G_{0^\circ}(\epsilon)$  at various strain loading. The numerical values are shown in Fig. 16. The Griffith's fracture criterion can be applied when  $J_1(\epsilon_c)$  exceeds the material surface energy  $2\gamma_s$ .

For mix mode fracture, the components of  $\mathbf{J}$  show distinct features.  $J_1(R)$  is path independent given that the  $x$ -axis of the local coordinate aligns with the fracture. The numerical values of  $J_1(R)$  is shown in Fig. 17 together with  $G_{0^\circ}$ . The relationship of  $J_1$  being equal to  $G_{0^\circ}$  from Eq. 17 with  $\theta = 0$  still holds, where we only see around 1% error. However,  $J_2(R)$  is not path independent. The numerical values of  $J_2(R)$  is shown

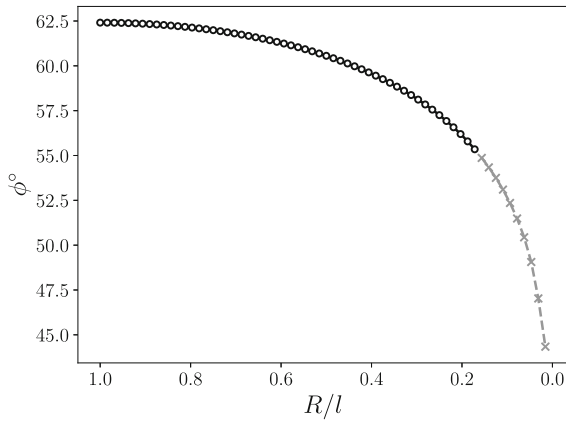


**Fig. 19** Directional angle  $\phi(R)$  given by  $\mathbf{J}$

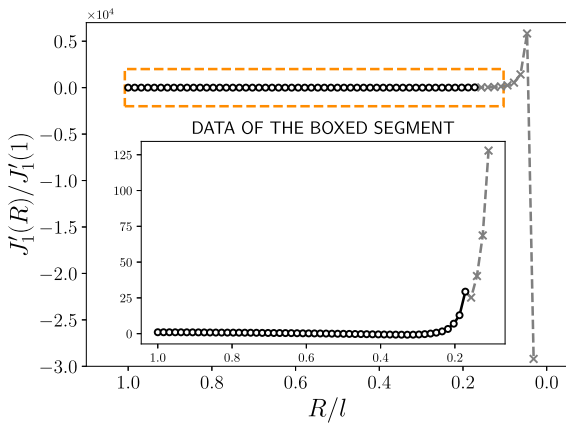


**Fig. 20** The numerical values of the numerical derivatives  $J'(R)$  of  $J(R)$  are shown

in Fig. 18, which shows a dependence on  $R$  i.e. where  $\Gamma$  intersects the fracture surface. One consequence of the  $J_2$  path dependency is the directional angle of  $\mathbf{J}$  is no longer a unique value which indicates the direction with maximum energy release rate. Instead, the directional angles have a wide range spanning from  $45^\circ$  to  $63^\circ$  as shown in Fig. 19.

$J_1(R)$  can be applied to best approximate the true  $J_2$  value which is at the limit of  $R \rightarrow 0$  in Eq. 14. However, we pointed out earlier in mode I fracture that the LEFM is broken with  $R \rightarrow 0$ . We observe the same with the numerical value of  $J_1(R)$  deviating from its constant. Here, we use the numerical gradient  $J'_1(R)$  to determine where the best possible intersection location can be i.e. beyond which the continuum limit of LSM is no longer elastic. When LEFM holds,  $J_1(R)$  fluctuates around a constant. We expect a small gradient  $J'_1(R)$  as

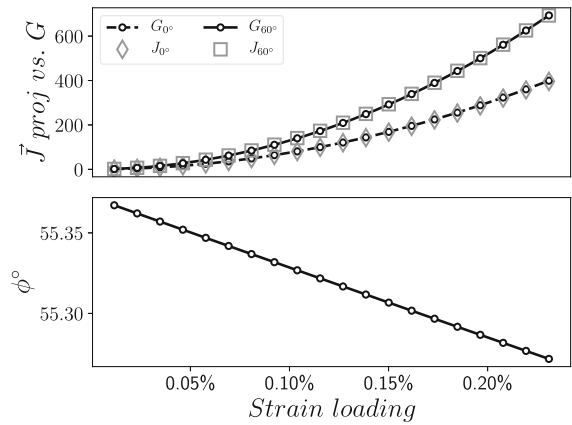


**Fig. 21** In the upper figure,  $J_0^\circ = J_1 \cos(0^\circ)$  and  $J_{60^\circ} = J_1 \cos(60^\circ) + J_2 \sin(60^\circ)$ . In the lower figure,  $\phi$  is given according to Eq. 18

shown in Fig. 20 within the boxed region marked with dark circles. Beyond the box region marked with gray cross, LEFM does not hold. We choose the last dark circle with  $R/l$  around 17% as the cut-off location. The resultant  $\mathbf{J}(\epsilon)$  with integration path intersecting the fracture surface at the cut-off location shows good agreement with  $G_{60^\circ}(\epsilon)$  and  $G_{0^\circ}(\epsilon)$  and the directional angle has a very small variation across strain loadings as can be seen in Fig. 21.

### 7 Energy release rate with uniform surface traction

We applied constant pressure to a mode I symmetrical and central crack. For comparison and validation purpose, the effective energy release rate  $G_e$  is calculated in three manners. They are a direct calculation as described in Sect. 5, a direct  $J^T$  integration as in Eq. 26 and a  $J^A$  approximation based on Eq. 28.

The directly calculated  $G_e$  and approximated  $J^A$  have minimal difference and are not sensitive to grid resolutions and applied pressure values. They cross validate each other as shown in Fig. 22. In the upper sub-figure of Fig. 22, the numerical values of both  $G_e$  and  $J^A$  remain the same constant with the doubling of grid resolution. It shows that the calculation of  $G_e$  is accurate even with a low grid resolution. In the lower sub-figure, with a higher applied surface pressure, the characteristics of  $G_e$  and  $J^A$  remain unaffected.

However, the directly integrated  $J^T$  shows a significant discrepancy with the directly calculated  $G_e$  and

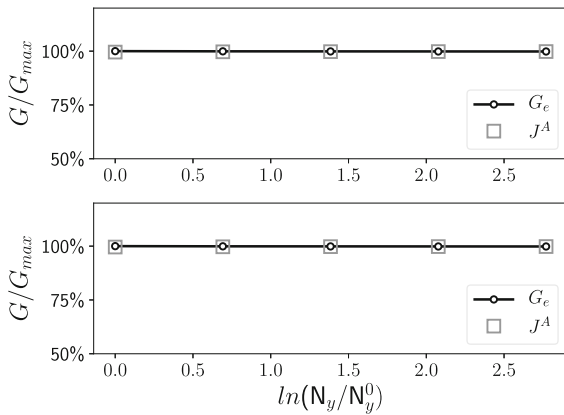


**Fig. 22** We show the numerical values of energy release rate  $G_e$  with a direct calculation and approximated  $J^A$  at various mesh resolution  $N_y$ . Two different pressure values were applied to the fracture surface. In the upper sub-figure, a lower level pressure was applied while in the lower sub-figure, a higher level one was applied. In both sub-plots, all values are normalized to its corresponding maximum  $G_e$  value

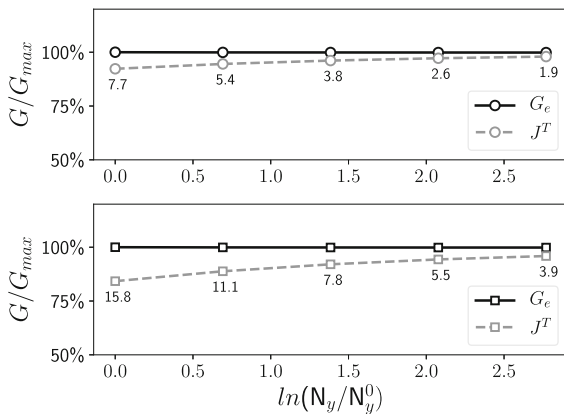


**Fig. 23**  $J^T$  is plotted together with  $G_e$  with respect to mesh density.  $J^T$  was calculated using the same surface pressure values and grid resolutions as those in Fig. 22

approximated  $J^A$  values. It has a strong dependency on the grid resolutions and applied pressure as shown in Fig. 23. Here, the boundary conditions are the same as those in Fig. 22. We define a relative error  $\delta_{int}$  between  $G_e$  and  $J^T$  as  $(G_e(N_y) - J^T(N_y))/G_e(N_y)$ . In Fig. 23, the error annotated by numbers in percentage decreases proportionally with  $1/\sqrt{N_y}$ . In addition, the relative error is bigger under a higher surface pressure at each corresponding grid resolution.

The relative error  $\delta_{int}$  is due to the inability to fully include all of the bonds on the fracture surface during numerical integration. As mentioned in Sect. 5, with

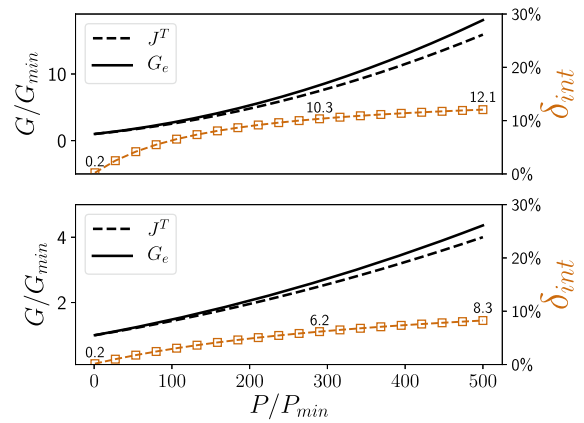


**Fig. 24** We ran a parametric study on the relative error defined as  $(G_e(P) - J^T(P))/G_e(P)$ . The parametric parameters are surface pressure  $P$  and external displacement loading  $u$ . In the upper fig, a lower external loading  $u_s$  is applied. While in the lower one, a higher one  $u_b$  is applied. At each external loading, a linear range of pressure  $P$  are applied and normalized to  $P_{min}$ . The annotated numbers of selected error are in percentage scale

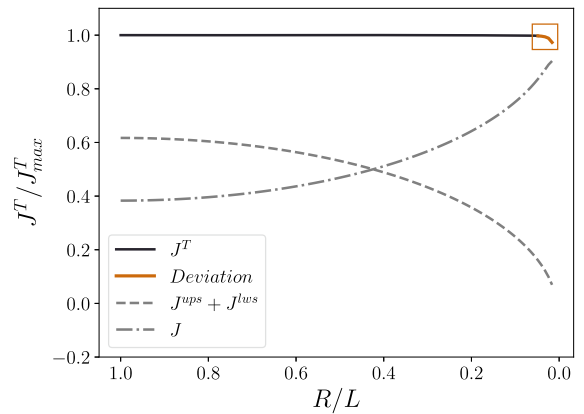


**Fig. 25** To verify the path independence of  $J^T$ , we calculated  $J^T$  values at various intersection locations of  $J$  path and fracture surface. We also present the components of  $J^T$  separately as  $J^{ups} + J^{lws}$  and  $J$ . All of the  $J$  values are normalized to the maximum value of  $J^T$

pressure included, a newly defined  $J$  path comprises of two parts. The first part is the conventional  $J$  path surrounding the fracture and it normally intersects the fracture surface away from the fracture tip. The second part is portion of the fracture surface starting from the intersection of conventional  $J$  path with fracture surface and ending at the middle of the bond with the fracture tip as its end. As a result, half of a bond is excluded in the numerical integration. The exclusion is necessary due to the singularity at the fracture tip.



With the increase of grid resolution, the length of the excluded half bond is effectively shortened. So that the relative error minimizes.

To further show the dependency of  $\delta_{int}$  on the values of the applied pressure, a parametric study is included here. As indicated in Fig. 24 by an orange dash line, initially,  $\delta_{int}$  increases with pressure. Then, it converges to a constant. Meanwhile, we applied two levels of external displacement loading on the grid and show the numerical results individually in the upper sub-fig with a smaller value and the lower one with a bigger value. The relative error decreases with the increase of external displacement loading. It is because the influence of pressure on the energy release rate is less significant in comparison with a bigger external displacement loading.

$J^T$  is largely path independent. As shown in Fig. 25,  $J^T$  remains a constant as long as the intersection of  $J$  path with fracture surface is a few bonds away from the fracture tip. It only deviates when the calculation of  $J^T$  has  $R$  within 5 percent of the fracture half length  $l$ , where  $R$  indicates the distance between intersection of  $J$  path with fracture surface and fracture tip. The components of  $J^T$  such as the surface integral  $J^{ups} + J^{lws}$  and  $J$  vary significantly along the fracture surface.

In order to compare the accuracy of the directly calculated  $G_e$  and direct integrated  $J^T$  along a propagation path,  $G_e(L')$  and  $J^T(L')$  are calculated at varying fracture length  $L'$ .  $G_e(L')$  and  $J^T(L')$  follows the same trend with respect to propagation length  $L'$  as shown in Fig. 26. The relative error  $\delta_{int}(L')$  remains. But, it decays exponentially initially when  $L'$  is small and quickly converges to a constant as shown in Fig. 27. The error is relatively big initially when the fracture starts to propagate. It is because limited bonds make up the fracture surface. The numerical integration  $J^T$  on the fracture surface is not accurate.

In addition, the components of  $G_e$  show a consistent ratio despite of fracture length. The mechanical component  $G_w$  and elastic components  $G$  of  $G_e$  are shown individually in Fig. 26, where the ratios  $G_w(L')/G_e(L')$  and  $G(L')/G_e(L')$  remain the same along the whole propagation length. In the case shown in Fig. 26, the ratio of the mechanical component  $G_w(L')/G_e(L')$  is 79.2% and correspondingly the elastic component  $G(L')/G_e(L')$  is 20.8%. While the components of  $J^T$  namely  $J^s$  and  $J$  do not correspond to the elastic and mechanical component of  $G_e$ .

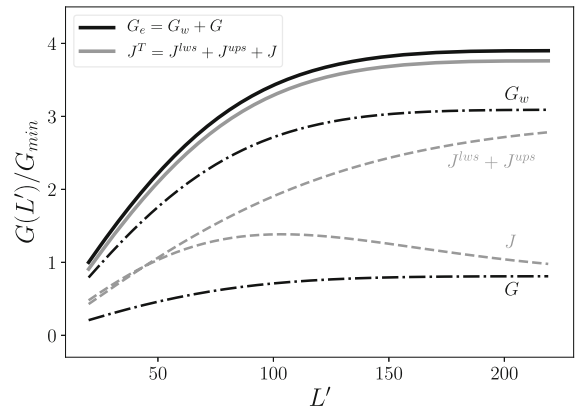


**Fig. 26** We propagated a mode I fracture in the fracture axial direction. The crack had an initial length of  $L_0$ . The propagated length of the fracture is  $L' = (L - L_0)/l$ , where  $L$  is the overall length and  $l$  is the bond length. Here, we present two groups of data. Data group 1 is the  $G_e(L')$  and its components  $G_w(L')$  and  $G(L')$ . Data group 2 is  $J^T(L')$  and its components  $J^{ups} + J^{lws}$  and  $J$

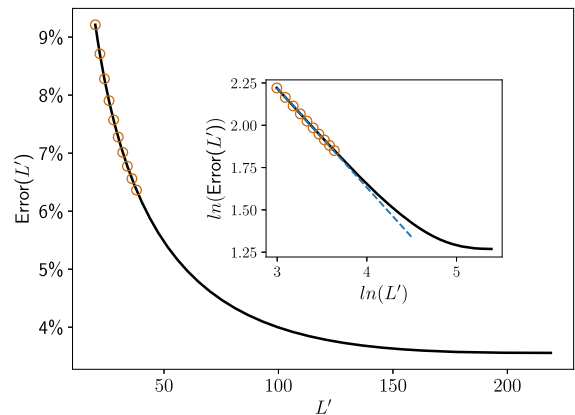


**Fig. 27** we show the relative error defined as  $(G_e(L') - J^T(L'))/G_e(L')$ . The figure in figure shows the  $\ln - \ln$  plot of the error and propagated length  $L'$ . The linear portion is labeled with orange  $\circ$  and at the same time, the same portion is labeled in the main figure

### 8 Numerical modeling of the sub-critical crack growth

Sub-critical fracture is a type of stable crack (Røyne et al 2011), where the crack front of the sub-critical fracture propagates with a finite, small and controllable velocity  $v$ . An energy gradient  $\Delta G$  defined as the difference between the effective energy release rate  $G_e$  and fracture surface energy  $2\gamma_s$  dictates the crack velocity. Due to the retraction of an energy gradient, an activated crack may halt or heal. Based on the reaction

rate theory, the crack velocity is modeled by a hyperbolic function of  $\Delta G$  as shown below (Wan et al 1990; Røyne et al 2011).

$$v = v_0 a_0 \exp\left(-\frac{\Delta F}{kT}\right) \sinh\left(\frac{\alpha \Delta G}{kT}\right). \quad (29)$$

where  $\Delta G$  is equal to  $(G_e - 2\gamma_s)$ ,  $k$  is the Boltzmann constant,  $T$  is the temperature in kelvin,  $v_0 = \frac{kT}{h}$  is the lattice vibration frequency,  $\Delta F$  is the quiescent value of the energy barrier and  $a_0$  is the characteristic atomic spacing (Røyne et al 2011).

Our modeling approach is to propagate the lattice spring model by a length  $\Delta L$  and calculate the effective energy release rate  $G_e(L)$ . Then, the calculation of the crack velocity is according to Eq. 29 by substituting  $G_e(L)$ . As an example, we first started with a small displacement loading to a sample with a dry crack of original length  $L_0$ . A dry crack refers to cracks without applied pressure. Subsequently, we measured the elastic energy release rate  $G(L_0)$  and compared it with a known surface energy  $2\gamma_s$ . If  $G(L_0)$  is smaller than  $2\gamma_s$ , the displacement loading underwent repeated increment until  $G(L_0)$  was equal or bigger than  $2\gamma_s$ . Under the critical displacement loading  $u_0$ , the crack propagated a length of  $\Delta L$ . At the same time, we kept track of the overall elastic energy  $E(L)$  of the sample and calculate  $G(L)$  according to Eq. 12. In this case, the effective energy release rate  $G_e$  is solely the elastic energy release rate  $G$ . The energy gradient  $\Delta G$  is  $G - 2\gamma_s$  and crack velocity is given by Eq. 29. The corresponding velocity profile labeled by orange line is shown in the upper part of Fig. 28. With the propagation of the crack, the elastic energy release rate also increases. As a result, the crack propagation accelerates. However, the elastic energy release rate eventually reaches its steady value even if the crack continues growing. So the crack maintains its velocity and the range of velocity only occupies part of the possible range based on the reaction rate theory.

As indicated by the blue solid line in the upper sub-figure of Fig. 28, the effects of pressure on the sub-critical fracture are twofold. First, it increases the activation velocity. Second, the average velocity is higher than the dry case or with a smaller applied pressure. With the displacement loading kept the same as the activation  $u_0$  of the dry crack, the inclusion of pressure introduces additional mechanical work  $G_w$ . It accelerates the crack growth.

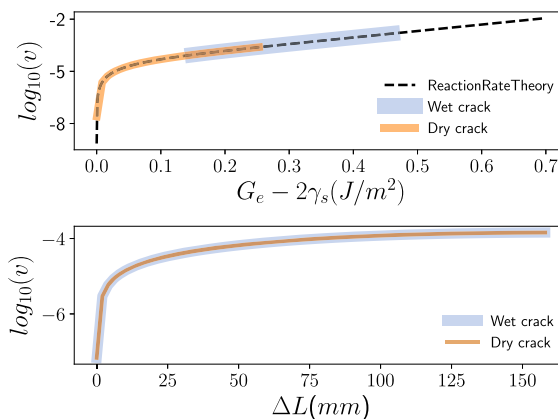


**Fig. 28** In the upper fig, the curve labeled as the reaction rate theory is a fit from experiment in Røyne et al (2008) according to crack velocity function  $v = v_0 a_0 \exp(-\frac{\Delta F}{kT}) \sinh(\frac{\alpha \Delta G}{kT})$ . The fitting parameters are  $\alpha = 2.9e-20 \text{ m}^2$  and  $\Delta F = 7.6e-20 \text{ J}$ . The temperature was  $22^\circ \text{C}$ . For the dry crack, the boundary condition is solely a displacement loading  $u_0$ . While for the wet crack, the boundary conditions are the same displacement loading  $u_0$  as dry crack coupled with a pressure of  $0.05 \text{ MPa}$  applied on the fracture surface. In the lower sub-fig, the dry crack has a displacement loading  $u_0$  as the boundary condition. The wet crack has a lower displacement loading  $u_1$  and a proper pressure such that the activation energy release rate  $G_e(L_0)$  is the same as  $G(L_0)$  of the dry crack

A dry crack and a wet crack with pressure applied can effectively be identical sub-critical fracture in terms of crack velocity and effective energy release rate. By only lowering the displacement loading of the wet crack while keeping  $u_0$  the same for the dry crack, the activation energy release rate  $G_e(L_0)$  of the wet crack was adjusted to match  $G(L_0)$  of a dry crack as well as surface energy  $2\gamma_s$ . Then, both of the dry and wet crack propagated a length of  $\Delta L$ . The resultant crack front velocity profiles are shown in the lower sub-figure of Fig. 28. It indicates that, at any crack length  $L$ ,  $G_e(L)$  is equal to  $G(L)$ . Consequently, the crack velocity  $v_{wet}(L)$  of the wet crack is also equal to  $v_{dry}(L)$  of the dry crack.

The geometrical differences of the effective cracks are small and differ only in the axial direction. As shown in Fig. 29, the surface of wet crack overlaps the one of the dry crack. The lateral geometrical difference  $\delta x_i$  defined as  $x_i^{wet} - x_i^{dry}$  is numerically insignificant as shown in Fig. 30, where  $i$  is the ID of a node on the fracture surface. However, the axial difference  $\delta y_i$  increases linearly with  $i$ . The effects of the pressure are twofold. On one hand, the normal component expands

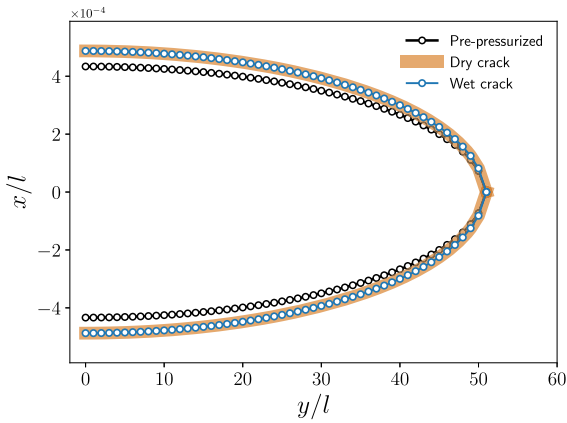


**Fig. 29** Fracture cavity geometries

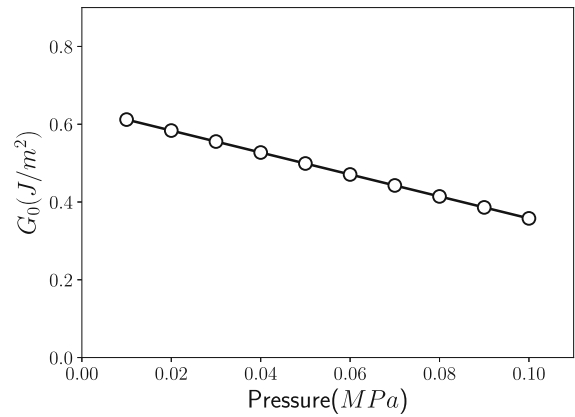


**Fig. 31** Pressure as a weakening agent

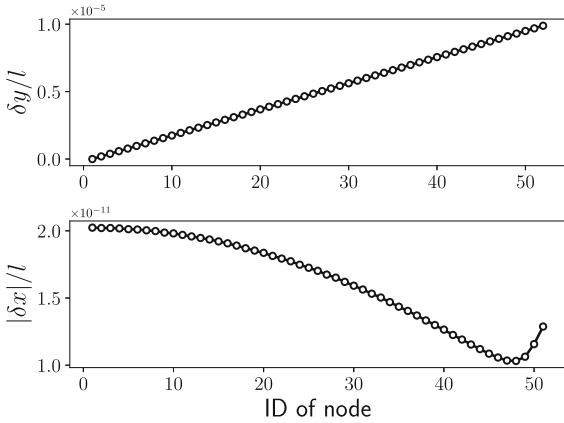


**Fig. 30** Lateral and axial difference

the pre-pressurized crack labeled by dark  $\circ$  in Fig. 29 to match with the dry crack laterally. On the other hand, the tangential component further elongates the wet cavity linearly along the surface. The closer to the fracture tip, the further the elongation is.

Pressure may be interpreted as a weakening agent to the fracture strength. Alternatively, the energy gradient can be rearranged as  $\Delta G = G - (2\gamma_s - G_w)$ .  $2\gamma_s$  and  $G_w$  together define a new effective surface energy  $\gamma_s^e$ . The bigger the pressure, the weaker the crack becomes. The critical elastic energy release rate  $G_0$  for the activation of a weakened crack decreases linearly with applied pressure as shown in Fig. 31.

### 9 Conclusion

In this study, we have introduced two equivalent energy based fracture criteria for the node-splitting LSM network. These fracture criteria are a direct energy release rate calculation and, for comparison and validation purpose, a  $J$ -integral implementation. The direct energy release rate is based on the virtual crack extension method and the implementation of  $J$ -integral in LSM is straight forward in LSM. They both show good agreement on the energy release rate calculation for the mode I fractures. For mode II fractures, the  $J_2$  component of vector  $J_i$  shows path dependency as elsewhere. As a result, the  $J_2$  component causes the predicted energy release rate and fracture direction deviating from those of the direct calculation. We followed Eischen (1987) to choose suitable  $J$  path to minimize the discrepancy.

These energy based fracture criteria enable LSM to study a wider ranges of physical processes, whose behavior depends on the energy release rate of the system. As an example, in this study, we are able to calculate the speed profile of the sub-critical fracture based on the reaction rate theory. The node-splitting LSM network coupled with the implemented fracture criteria provides accurate energy release rate to enable the calculation.

The coupling scheme of a static pressure with iterative Newton–Raphson introduced here can be further extended to include other processes. For one example, instead of a static pressure, a full fluid solver can be coupled to the iterative Newton solver by following the same principle using node-splitting LSM as described in Sect. 4. The static pressure impacts significantly on

the energy release rate calculation in terms of  $J$ -integral implementation.  $J$ -integral shows a strong dependency on mesh resolution. A fine mesh around the fracture tip is required to yield satisfactory results. However, the direct calculation of effective energy release rate with mechanical energy component due to the static pressure is still accurate. By making use of the accurate effective energy release rate, the static pressure is shown to be a weakening agent on the strength of the sub-critical fracture with applications such as hydro-fracture.

The improvement of the elastic state of the fracture tip such as the grid dependency of stress may be of interest for future study. The abnormality of the stress at the fracture tip may be due to large rotation of bonds with grid size dependence. A local criterion may be possible through techniques such as non-linear analysis as compared to current linear analysis, or cohesive zone model which creates a smooth crack tip for analysis.

**Acknowledgements** This project is part of the Nanoheal project. Nanoheal project has received funding from the European Union's Horizon 2020 research and innovation programme under the Marie Skłodowska-Curie Grant Agreement No. 642976.

**Funding** Open access funding provided by University of Oslo (incl Oslo University Hospital).

#### Declarations

**Conflict of interest** The authors have no competing interests to declare that are relevant to the content of this article.

**Open Access** This article is licensed under a Creative Commons Attribution 4.0 International License, which permits use, sharing, adaptation, distribution and reproduction in any medium or format, as long as you give appropriate credit to the original author(s) and the source, provide a link to the Creative Commons licence, and indicate if changes were made. The images or other third party material in this article are included in the article's Creative Commons licence, unless indicated otherwise in a credit line to the material. If material is not included in the article's Creative Commons licence and your intended use is not permitted by statutory regulation or exceeds the permitted use, you will need to obtain permission directly from the copyright holder. To view a copy of this licence, visit <http://creativecommons.org/licenses/by/4.0/>.

#### References

- Anderson TL (2017) Fracture mechanics: fundamentals and applications. CRC Press, Boca Raton. <https://doi.org/10.1201/9781315370293>
- Atkinson BK (1984) Subcritical crack growth in geological materials. *J Geophys Res Solid Earth* 89(B6):4077–4114. <https://doi.org/10.1029/JB089iB06p04077>
- Bolander J Jr, Saito S (1998) Fracture analyses using spring networks with random geometry. *Eng Fract Mech* 61(5–6):569–591. [https://doi.org/10.1016/S0013-7944\(98\)00069-1](https://doi.org/10.1016/S0013-7944(98)00069-1)
- Buxton GA, Verberg R, Jasnow D et al (2005) Newtonian fluid meets an elastic solid: coupling lattice Boltzmann and lattice-spring models. *Phys Rev E* 71(5):056–707. <https://doi.org/10.1103/PhysRevE.71.056707>
- Eischen J (1987) An improved method for computing the  $J_2$  integral. *Eng Fract Mech* 26(5):691–700. [https://doi.org/10.1016/0013-7944\(87\)90134-2](https://doi.org/10.1016/0013-7944(87)90134-2)
- Erdogan F, Sih G (1963) On the crack extension in plates under plane loading and transverse shear. *J Fluids Eng* 10(1115/1):3656897
- Flekkøy EG, Malthé-Sørenssen A, Jamtveit B (2002) Modeling hydrofracture. *J Geophys Res Solid Earth* 107(B8):ECV-1. <https://doi.org/10.1029/2000JB000132>
- Freiman S (1984) Effects of chemical environments on slow crack growth in glasses and ceramics. *J Geophys Res Solid Earth* 89(B6):4072–4076. <https://doi.org/10.1029/JB089iB06p04072>
- Griffith AA (1921) VI. The phenomena of rupture and flow in solids. *Philos Trans R Soc Lond Ser A Contain Pap Math Phys Charact* 221(582–593):163–198. <https://doi.org/10.1098/rsta.1921.0006>
- Hafver A, Jettestuen E, Feder J et al (2014) A node-splitting discrete element model for fluid-structure interaction. *Physica A* 416:61–79. <https://doi.org/10.1016/j.physa.2014.08.039>
- Hellen T (1975) On the method of virtual crack extensions. *Int J Numer Methods Eng* 9(1):187–207. <https://doi.org/10.1002/nme.1620090114>
- Karlsson A, Bäcklund J (1978)  $J$ -integral at loaded crack surfaces. *Int J Fract* 14(6):R311–R318. <https://doi.org/10.1007/BF00116006>
- Knowles JK, Sternberg E (1972) On a class of conservation laws in linearized and finite elastostatics. *Tech Rep*. <https://doi.org/10.1007/BF00250778>
- Kosteski L, Barrios D'Ambrá R, Iturrioz I (2012) Crack propagation in elastic solids using the truss-like discrete element method. *Int J Fract* 174:139–161. <https://doi.org/10.1007/s10704-012-9684-4>
- Landau L, Lifshitz E (1986) Theory of elasticity, volume 7 of course of theoretical physics, 3. <https://doi.org/10.1063/1.3057037>
- Lifeng M, Korsunsky AM (2005) On the use of vector  $J$ -integral in crack growth criteria for brittle solids. *Int J Fract* 133(4):L39–L46. <https://doi.org/10.1007/s10704-005-0631-5>
- Malthé-Sørenssen A, Walmann T, Feder J et al (1998) Simulation of extensional clay fractures. *Phys Rev E* 58(5):5548. <https://doi.org/10.1103/PhysRevE.58.5548>
- Martins AF, Bennett NC, Clavel S et al (2018) Locally-curved geometry generates bending cracks in the African elephant skin. *Nat Commun* 9(1):1–8. <https://doi.org/10.1038/s41467-018-06257-3>
- Meakin P (1987) A simple model for elastic fracture in thin films. *Thin Solid Films* 151(2):165–190. [https://doi.org/10.1016/0040-6090\(87\)90231-8](https://doi.org/10.1016/0040-6090(87)90231-8)

- Norton A, Turk G, Bacon B et al (1991) Animation of fracture by physical modeling. *Vis Comput* 7(4):210–219. <https://doi.org/10.1007/BF01900837>
- Ostoja-Starzewski M (2002) Lattice models in micromechanics. *Appl Mech Rev* 55(1):35–60. <https://doi.org/10.1115/1.1432990>
- Rice JR (1968) A path independent integral and the approximate analysis of strain concentration by notches and cracks. *J Appl Mech* 35(2):379–386. <https://doi.org/10.1115/1.3601206>
- Rice J, Budiansky B (1973) Conservation laws and energy-release rates. *J Appl Mech* 40:201–203. <https://doi.org/10.1115/1.3422926>
- Røyne A, Jamtveit B, Mathiesen J et al (2008) Controls on rock weathering rates by reaction-induced hierarchical fracturing. *Earth Planet Sci Lett* 275(3–4):364–369. <https://doi.org/10.1016/j.epsl.2008.08.035>
- Røyne A, Bisschop J, Dysthe DK (2011) Experimental investigation of surface energy and subcritical crack growth in calcite. *J Geophys Res Solid Earth*. <https://doi.org/10.1029/2010JB008033>
- Sadd MH (2009) Elasticity: theory, applications, and numerics. <https://doi.org/10.1016/C2012-0-06981-5>
- Schlangen E, Garboczi E (1996) New method for simulating fracture using an elastically uniform random geometry lattice. *Int J Eng Sci* 34(10):1131–1144. [https://doi.org/10.1016/0020-7225\(96\)00019-5](https://doi.org/10.1016/0020-7225(96)00019-5)
- Selle A, Lentine M, Fedkiw R (2008) A mass spring model for hair simulation. In: *ACM SIGGRAPH 2008 papers*, pp 1–11. <https://doi.org/10.1145/1360612.1360663>
- Swanson PL (1984) Subcritical crack growth and other time-and environment-dependent behavior in crustal rocks. *J Geophys Res Solid Earth* 89(B6):4137–4152. <https://doi.org/10.1029/JB089iB06p04137>
- Wan KT, Lathabai S, Lawn BR (1990) Crack velocity functions and thresholds in brittle solids. *J Eur Ceram Soc* 6(4):259–268. [https://doi.org/10.1016/0955-2219\(90\)90053-1](https://doi.org/10.1016/0955-2219(90)90053-1)
- Wu TH, Qi D (2017) Lattice-Boltzmann lattice-spring simulations of influence of deformable blockages on blood fluids in an elastic vessel. *Comput Fluids* 155:103–111. <https://doi.org/10.1016/j.compfluid.2017.03.029>
- Zhang Z, Ding J, Ghassemi A et al (2015) A hyperelastic-bilinear potential for lattice model with fracture energy conservation. *Eng Fract Mech* 142:220–235. <https://doi.org/10.1016/j.engfracmech.2015.06.006>

**Publisher's Note** Springer Nature remains neutral with regard to jurisdictional claims in published maps and institutional affiliations.